Cathepsin K as a Key SARS-CoV-2 Cell Entry Protease and Dual-Inhibition Target

S. Yasin Tabatabaei Dakhili[1,#], Dipon Saha[1,#] ,Preety Panwar[1], Eliot Mar[1], Olivier Hinse[2], Yu Seby Chen[2], Bryan J. Fraser[4,5], Cheryl Arrowsmith[4,5] , Masahiro Niikura[3] , Filip Van Petegem[2], Dieter Brömme[1,2,*]

[1]Department of Oral Biological & Medical Sciences, Faculty of Dentistry, The University of British Columbia; Vancouver, Canada. [2] Department of Biochemistry and Molecular Biology, Faculty of Medicine, The University of British Columbia; Vancouver, Canada. [3]Faculty of Health Sciences, Simon Fraser University, Burnaby, Canada.[4] Department of Medical Biophysics, University of Toronto, Toronto, Canada. [5]Structural Genomics Consortium Toronto, Toronto, Canada.

[#] authors contributed equally

[*]Corresponding author. Email: dbromme@dentistery.ubc.ca

Abstract:

SARS-CoV-2 relies on host proteases to cleave and activate its spike protein for cell entry through either the endosomal or plasma membrane pathway. Although cysteine cathepsins are known to mediate the endosomal route, the identity of the dominant enzyme has remained unclear. Here, we identify human Cathepsin K (hCatK), a lysosomal cysteine protease, as a previously unrecognized but functionally important mediator of viral entry. While human Cathepsin L (hCatL) has long been regarded as the principal endosomal protease, inhibition of hCatK with the selective inhibitor Odanacatib suppressed viral propagation in endothelial cells as effectively as the broad-spectrum cysteine protease inhibitor E-64d, implicating hCatK as a key driver of endosomal entry. Enzymatic profiling further revealed that hCatK exhibits 25- to 70-fold higher catalytic efficiency at the Furin cleavage site (FCS) compared to hCatL and displays a distinct cleavage pattern in the Omicron FCS relative to the Wuhan variant. We also demonstrate

that hCatK is a submicromolar (0.6 ± 0.1 μM) off-target of Nirmatrelvir, a clinically approved 3CL-Mpro inhibitor, and present a high-resolution crystal structure of the hCatK–Nirmatrelvir complex that informs rational design of dual-acting antivirals. Collectively, these findings redefine the landscape of host proteases in SARS-CoV-2 entry and establish hCatK as an overlooked yet strategic target for antiviral intervention.

Introduction

The continued evolution of SARS-CoV-2, particularly Omicron and its subvariants, has compromised the effectiveness of existing vaccines and antiviral therapies by enabling immune escape and reducing drug susceptibility [1-4]. These challenges underscore the need for antiviral strategies that are resilient to viral mutation. One promising approach is to target host factors essential for viral entry and replication, which are generally more conserved and less prone to selective pressure [5-8]. Host proteases are critical for SARS-CoV-2 entry, as they cleave the spike (S) protein at defined sites to enable membrane fusion [9,10]. The roles of Furin and TMPRSS2 in facilitating SARS-CoV-2 entry through the plasma membrane, as well as Cathepsin L (CatL) through the endosomal entry route have been partly characterized [11-16]. Yet the contribution of other endolysosomal cysteine cathepsins remains poorly defined, because most studies lacked quantitative enzymatic analyses or relied on broad-spectrum inhibitors that obscure protease-specific functions. Addressing this gap could uncover new therapeutic targets and inform the development of antivirals with broader efficacy [17-19]. Cathepsin K (CatK) has emerged as a notable candidate, as its selective inhibitor ONO-5334 ranked among the top compounds with antiviral activity against SARS-CoV-2 in a large drug-repurposing screen [20]. CatK is also highly expressed in lung and vascular tissues including endothelial cells, key sites of viral infection [21-24]. Despite these observations, its role in viral entry has not been investigated.

Here, we show that CatK is a functionally important protease in SARS-CoV-2 entry and a potential target for host-directed therapy. In this study, we investigate the enzymatic activity of hCatK relative to other cathepsins and canonical convertases, evaluate its inhibition by Nirmatrelvir [25], a clinically approved 3CL-Mpro protease inhibitor, and resolve the structural basis of CatK-Nirmatrelvir interaction. These findings provide mechanistic

insight into the role of CatK in viral pathogenesis and support the rationale for dual-acting antivirals that target both viral and host proteases.

Materials and Methods:

FRET-based peptides, Ac-AE(Edans)QTNSPRRARSVK(Dabcyl) (FCS-Wu), Ac-AE(Edans)QTKSHRRARSVK(Dabcyl) (FCS-Omic), and Ac-AE(Edans)LPDPSKPSKRSFIK(Dabcyl) (TSC), were custom synthesized (>98% purity) by Biomatik Co., Ontario, Canada. Recombinant SARS-CoV-2 Spike proteins S1 and S2 were purchased from RayBiotech Life Inc. (GA, USA). Human CatK antibody (Abcam; AB37259) and Alexa Fluor dye 488 (Abcam; AB112125) were obtained from Abcam (Cambridge UK), and viral nucleocapsid protein antibody (GTX635674) from GeneTax (Irvine, CA). Amicon® Ultra - 15 Centrifugal Filters were from Merck Millipore Ltd, Irland). Human cathepsins K was expressed in *Pichia pastoris* and purified as described in [26] and human cathepsin S was expressed in *E. coli* BL21(DE3) [27]. Recombinant TMPRSS2 (dasTMPRSS2) was produced and purified as previously described [28]. Human recombinant cathepsin B had been kindly provided by J. Mort† from the Shriner's Hospital for Sick Children (Montreal, QC, Canada). Recombinant human Furin and human liver cathepsin L were obtained from Fisher Scientific, Canada. Furin Inhibitor I (Decanoyl-RVKR-CMK) was obtained from EDM Millipore Corp., USA, L-3-carboxy-*trans*-2–3-epoxypropionyl-leucylamido-(4-guanidino)-butane ethyl ester (E-64d) from Sigma-Aldrich (Sigma-Aldrich Canada, Oakville, Ontario, Canada), Odanacatib, Camostat from Selleck Chemicals (Houston, TX) and Nirmatrelvir from A2B Chem, LLC (San Diego, CA).

SARS-CoV-2 virus propagation

SARS-related Coronavirus 2 (SARS-CoV-2), isolate USA-WA1/2020, was obtained from BEI Resources (Cat# NR-52281) and used in all experiments. All work with SARS-CoV-2 was conducted in BSL-3, a Containment Level 3 facility at Simon Fraser University, following approved protocols (SFU Biosafety Committee Permit #361-2022 and #361-2023). The stock virus was produced by amplifying the initial seed virus in VeroE6/TMPRSS2 cells (JCRB Cell Bank, Cat# JCRB1819) through two passages before use in experiments.

Endothelial cell culture and virus infection

EA.hy 926 endothelial cells (ATCC, Burlington, ON) were seeded at a density of 50,000 cells per well in Dulbecco's Modified Eagle Medium (DMEM) containing 10% fetal bovine serum in a multi-well plate and infected with 50,000 pfu of the virus in 50 µL of culture medium added to the existing medium and incubated at 37°C for 48 hours at 5% CO_2 in the presence or absence of E-64d, Camostat, Odanacatib or Nirmatrelvir (0 to 20 µM). Following treatment and removing the medium, cells were scraped into 200 µL of RIPA containing a proteinase inhibitor cocktail (ThermoFisher Scientific, Canada) and incubated for 10 min on ice with occasional vortex mixing for the Western blot samples. The samples were boiled before being removed from BSL-3. For microscopic studies, the cells were fixed in 0.2% glutaraldehyde and 4% formalin (1 mL per well) for 30 min at room temperature after removing the medium. The plates were disinfected and removed from BSL-3 for staining.

Immunostaining for hCatK was performed using a protocol optimized for fixed cell imaging. In parallel, viral nucleocapsid protein staining was carried out using a specific antibody to detect infection levels. Briefly, 0.2% glutaraldehyde and 4% formalin fixed EA.hy 926 cells were permeabilized using 0.1% Triton X-100. After blocking with 1% bovine serum albumin (BSA), cells were incubated with primary antibodies against CatK and viral nucleocapsid protein, followed by fluorescently labeled secondary antibodies (Alexa Fluor 647; ThermoFisher Scientific, Canada). Actin cytoskeleton was stained using Phalloidin conjugated to dye (Alexa Fluor 488), and nuclei were counterstained with DAPI. Imaging was performed using a fluorescence microscope (Olympus BX61 Fluorescence microscope, Olympus, USA).

3CL-Mpro protein expression and purification

Hisx6-tagged WT- 3CL-Mpro (expression vector kindly provided by Dr. C. Overall, UBC) was expressed in *E. coli* BL21-DE3. The inoculated culture (2–6 L) was grown in LB broth medium at 37°C in the presence of 100 microgram/L ampicillin till OD_{600nm} reached 0.6. The temperature was then lowered to 16°C, and expression was induced overnight with 0.5 mM IPTG. The cells were harvested by centrifugation at 5,000g at 15°C for 10 min in

an Avanti J-E centrifuge (Beckman Coulter, Inc) and resuspended in a lysis buffer (50 mM Tris [pH 7.5], 300 mM NaCl). The cells were lysed by sonication on ice and centrifuged at 20,000g for 30 min at 4°C. The supernatant was loaded on a Ni-NTA column previously equilibrated with a lysis buffer at RT. The His-tagged 3CL-Mpro enzyme was eluted from the column in 50 mM Tris, pH 7.5, 300 mM NaCl, 300 mM imidazole. The elution was buffer exchanged to 50 mM Tris, pH 7.5, 150 mM NaCl overnight in presence of PreScession protease to get rid of imidazole and His-tag. Then the enzyme was purified using the Ni-NTA column and finally, loaded onto a Superdex 200 size-exclusion column (GE Healthcare) using an AKTA purifier core system (GE Healthcare). The column was pre-equilibrated with a degassed filtered buffer (50 mM Tris [pH 7.5], 150 mM NaCl). The final protein was collected, concentrated and kept in -80 ºC for future use. To express Hisx6-tagged-PreScission protease (expression plasmid kindly provided by Dr. Petegem, UBC), the plasmid was inoculated with *E. coli* BL21-DE3 culture (2–6 L) and grown in LB broth medium at 37°C in the presence of 100 µg/L ampicillin till OD_{600nm} reach 0.6. The temperature was then lowered to 16°C, and expression was induced overnight with 0.5 mM IPTG. The cells were harvested by centrifugation at 5,000g at 15°C for 10 min in an Avanti J-E centrifuge (Beckman Coulter, Inc) and resuspended in a lysis buffer (50 mM Tris [pH 7.5], 300 mM NaCl). The cells were lysed by sonication on ice and centrifuged at 20,000g for 30 min at 4°C. The supernatant was loaded on a Ni-NTA column previously equilibrated with a lysis buffer at RT. The His-tagged PreScission enzyme was eluted from the column in 50 mM Tris, pH 7.5, 300 mM NaCl, 300 mM imidazole. Purified protein was kept at -80 ºC in presence of 5mM beta-mercaptoethanol until further use.

Enzyme kinetic assays

All enzyme assays were performed at room temperature. Cleavage of fluorogenic substrates was monitored using a BioTek Synergy H4 microplate reader. Active site titrations of cathepsins, TMPRSS2, and Furin were conducted using E-64d, Nafamostat, and Decanoyl-RVKR-CMK, respectively. To determine k_{cat} and K_M values, assays were performed at constant enzyme concentrations with increasing concentrations of FCS-Wu, FCS-Omic, and TCS substrates, respectively. Cathepsin assays were conducted in 0.1

M sodium acetate buffer (pH 5.5) containing 2.5 mM dithiothreitol (DTT) and 2.5 mM ethylenediamine-tetraacetic acid (EDTA). Cathepsins were used at final concentrations ranging from 10 to 400 nM, and substrate concentrations ranged from 0 to 90 μM. Furin assays were performed in 0.1 M HEPES buffer (pH 7.5) supplemented with 0.5% Triton X-100 and 1 mM $CaCl_2$. Furin was used at a final concentration of 10 nM, and substrate concentrations ranged from 0 to 60 μM. 3CL-Mpro assays were carried out in 0.05 M Tris-HCl buffer (pH 7.5) containing 10 mM DTT. The enzyme was used at a final concentration of 100 nM, with substrate concentrations ranging from 0 to 60 μM. TMPRSS2 assays were performed in 25 mM Tris buffer (pH 8.0) containing 75 mM NaCl and 2 mM $CaCl_2$ with a TMPRSS2 concentration of 12 nM, and substrate concentrations between 0 to 60 μM. All assays were performed in two independent experiments, each in triplicate. Data were plotted using the Michaelis–Menten model and analyzed via nonlinear regression in GraphPad Prism (Version 5.0, GraphPad Software, La Jolla, California, USA). Inhibition assays were conducted in the presence of increasing concentrations of Nirmatrelvir and Z-FR-AMC (5–30 μM) for cathepsins and MCA-AVLQSGFRK(Dnp)RR for 3CL-Mpro.

LC–MS/MS enzyme assays and LC–MS/MS data acquisition on TIMS-TOF Pro2:
FRET-based peptide substrates (50 μM) as listed above were added to the appropriate activity buffer corresponding to each enzyme. The enzyme was then added to the mixture, which was incubated at room temperature for 1 hour (CatK, S, L, B 5-400 nM; Furin 4 nM; and TMPRSS2 12 nM). The reaction was stopped by adding the corresponding inhibitor and 60% (v/v) methanol. The mixture was stored at –20 °C for 2 hours, followed by centrifugation at 21,000 × g for 10 minutes to remove the enzyme. Each reaction was performed in duplicate.

20 ng of peptide was injected and separated on-line using a NanoElute 2 UHPLC system (Bruker Daltonics) with Aurora Series Gen3 (CSI) analytical column, (25 cm x 75 μm 1.7 μm C18 120Å, with CSI fitting; Ion Opticks, Parkville, Victoria, Australia). The analytical column was heated to 50°C using a column toaster M (Bruker Daltonics). The NanoElute thermostat temperature was set at 7°C. Buffer A consisted of 0.1% aqueous formic acid and 0.5% acetonitrile in water, and buffer B consisted of 0.1% aqueous formic acid and 0.5% acetonitrile in water. Before each run, the analytical column was

conditioned with 4 column volumes of buffer A. The analysis was performed at 0.30 µL/min flow rate. A standard 30 min gradient was run from 2% B to 12% B over 15 min, then to 33% B from 15 to 30 min, then to 95% B over 0.5 min, held at 95% B for 7.72 min.

Liquid chromatography was coupled to a Trapped Ion Mobility - Time of Flight mass spectrometer with dual TIMS (TimsTOF Pro2; Bruker Daltonics). The Captive Spray ionization source was operated at 1600 V capillary voltage, 3L/min drying gas, and 200°C drying temperature. During analysis, the TIMS-TOF Pro 2 was operated with Parallel Accumulation-Serial Fragmentation (PASEF) scan mode for DDA acquisition. The MS and MS/MS spectra were collected in positive mode, from m/z 100 Th to m/z 1700 Th, and from ion mobility range (1/ K_0) 0.7 V*s/cm^2 to 1.3 V*s/cm^2. A polygon filter was applied to the mass-to-charge and the ion mobility plane to include the most likely peptide precursors and to reduce singly charged background ions.

TIMS-MS scan was set at equal ramp time and accumulation time of 100 ms, at a rate of 9.42 Hz (100% duty cycle). Active exclusion was enabled with a 0.05 min release and reconsidered if their intensity increased more than 4 times. For each TIMS cycle, 3 PASEF MS/MS scans were recorded (total cycle time 0.42 s). Target Intensity for parent ions was set to 10,000 cts/s with a threshold of 1,000 cts/s. Isolation widths were set at 2.07 m/z starting m/z 400 Th and 3.46 m/z ending m/z 1000 Th. The collision energy was ramped linearly as a function of mobility value from 27eV at 1/k0 = 0.7 V·s/cm^2 to 55 eV at 1/k0 = 1.35 V·s/cm^2.

Crystallization and structural analysis of Nirmatrelvir-hCatK complexes

Recombinant hCatK was expressed in *P. pastoris* and purified as previously described [26]. To obtain an Nirmatrelvir-hCatK complex, Nirmatrelvir was dissolved in DMSO to 50 mM and added to hCatK (1 mg/mL) in 100 mM sodium acetate pH 5.5, 2.5 mM DTT and 2.5 mM EDTA. The protein-inhibitor complex was then concentrated to 5 mg/mL using centrifugal filters with a 10 kDa molecular weight cutoff. Crystals of Nirmatrelvir-hCaK complexes were obtained by equilibrating 0.7 µL of the protein-inhibitor mixture and 0.7 µL of reservoir solution (0.96 M sodium citrate pH 7) in sitting-drop vapor diffusion system at 22 °C. Suitable crystals were formed within 3 weeks at room temperature. Crystals were fished out and incubated in a cryoprotectant solution (the cryoprotectant containing

1M sodium citrate, 25% Ethylene Glycol and 2 mM Nirmatrelvir) for 2 min before flash-frozen in liquid nitrogen for data collection.

Diffraction data from a single crystal were collected at 100 K with a wavelength of 0.98 Å using a DECTRIS EIGER2 XE 16M detector at beamline BL12-2 of the Stanford Synchrotron Radiation Lightsource (Menlo Park, California, USA). The dataset was processed with the program iMosflm version 7.2.1 [29] and the intensities scaled with SCALA [30] to a resolution of 1.62 Å for Nirmatrelovir-bound hCatK. Phasing was performed by molecular replacement using human wild-type CatK structure (PDB: 5TUN). The restraints for the complexed Nirmatrelvir were generated using ELBOW [31] and fitted into the model during refinement. All modeled structures were refined by cycles of automated refinement in PHENIX [32] COOT [33] in the PHENIX program suite. Structural images were prepared using PyMOL software (PyMOL Molecular Graphics System, Version 3 Schrödinger, LLC).

Results

Effect of cysteine protease inhibitors on the infection of endothelial cells with SARS-CoV-2

To understand the importance of cysteine cathepsins in endosomal entry, we used the EA.hy926 endothelial cell (EC) line as a model. This choice was based on the relatively low TMPRSS2 expression in ECs [34], suggesting that viral infection in these cells likely relies considerably on the endosomal pathway [35]. Interestingly, a comparison between SARS-CoV-2 Wuhan variant-infected ECs (Fig. 1A) and uninfected controls (Fig. 1B) revealed a 7-fold upregulation of hCatK (Fig. 1C). To investigate the potential specific role of hCatK in this process, we treated ECs with Odanacatib, a selective hCatK inhibitor, along with E-64d, a broad-spectrum cysteine cathepsin inhibitor (Fig. 1D). In addition, cells were treated with the TMPRSS2 inhibtior, Camostat, and the 3CL-Mpro inhibitor, Nirmatrelvir. Viral infection was measured by quantifying the percentage of ECs positive for intracellular nucleocapsid protein. All four inhibitors, E-64d, Odanacatib, Camostat, and Nirmatrelvir, reduced infection in a dose-dependent manner (Fig. 1C). Interestingly, E-64d and Odanacatib showed similar inhibitory effects, with EC_{50} values of 7.5 ± 2.2 μM and 9.0 ± 2.6 μM, respectively (Fig. 1F), suggesting that hCatK is the dominant

contributor to viral cell entry among cathepsins. Camostat, a TMPRSS2 inhibitor, also showed a similar potency (EC_{50} of 6.1 ± 2.2 μM) as E-64d and Odanacatib, indicating that both the endolysosomal and cell-membrane entrance pathway were used to a comparable extent by SARS-CoV2 in this EC line. Nirmatrelvir, developed as a highly selective inhibitor of 3CL-Mpro [25], demonstrated a 3- to 4-fold greater potency in this assay with an EC_{50} of 2.2 ± 0.4 μM in preventing the proliferation of the virus. These findings suggest that hCatK plays a dominant role in mediating SARS-CoV-2 entry into ECs.

Kinetic analysis of Furin, TMPRSS2, and cysteine cathepsins using substrates representing processing sites in SARS-CoV-2 spike proteins

To clarify the specific contributions of cysteine cathepsins to SARS-CoV-2 Spike protein processing, we designed three Förster resonance energy transfer (FRET)-based substrates corresponding to the wild-type Wuhan FCS Furin cleavage site (FCS-Wu), the Omicron FCS (FCS-Omic), and the TMPRSS2 cleavage site (TCS) (Fig. 2A). Kinetic parameters were measured for four major human cysteine cathepsins (CatK, S, L, and B), alongside TMPRSS2 and Furin, which represent proteases related to the endosomal and plasma membrane viral entrance pathways, respectively.

The results showed the highest catalytic efficiency for Furin for both FCS-Wu and FCS-Omic (k_{cat}/K_M= 2,288 and 2,976 $mM^{-1}\ s^{-1}$, respectively). Human Cathepsin B (hCatB) cleaved both FCS-Wu and FCS-Omic substrates (k_{cat}/K_M - 218 and 265 $mM^{-1}\ s^{-1}$, respectively) at levels comparable to TMPRSS2 (k_{cat}/K_M - 277 and 300 $mM^{-1}\ s^{-1}$, respectively). Notably, hCatK displayed between 58 to 64-fold higher catalytic efficiency for FCS-Wu compared to hCatS and hCatL (Fig. 2B,C). Also, hCatK showed 24- and 140-fold higher catalytic efficiency for FCS-Omic compared to hCatL and hCatS. For the TCS substrate, hCatB hydrolyzed the site with ~1.9-fold higher catalytic efficiency than TMPRSS2, whereas hCatK remained a competent enzyme but operated at ~3.6-fold lower efficiency than TMPRSS2. Furin and CatL exhibited only trace activity toward TCS (Fig. 2D).

These data indicate that among cysteine cathepsins, hCatB and hCatK display substantial catalytic capacity for both FCS and TCS substrates, in some cases

approaching or exceeding the activity of TMPRSS2. Given the exclusive reliance of endosomal viral entry on cathepsins, tissues with high CatB and CatK expression are likely to use these enzymes as dominant endosomal proteases that activate the Spike protein and thereby facilitate viral entry.

LC-MS/MS analysis of protease cleavage sites using the substrate representing the TCS and FCS from Wuhan and Omicron SARS-CoV-2

Proteolytic activation of the spike protein at FCS and TCS is a critical step in deriving membrane fusion events required for SARS-CoV-2 infectivity [36]. Although multiple host proteases have been implicated, their exact cleavage preferences at the FCS and TCS remain unclear. Defining these patterns is essential to assign enzymatic activity unambiguously and distinguish overlapping or alternative processing events. We therefore performed LC–MS/MS analysis using FRET-based synthetic peptide substrates corresponding to FCS-Wu, FCS-Omic, and TCS. To confirm the cleavage patterns observed with synthetic peptides, we performed complementary LC-MS/MS analysis using the full-length recombinant S1 and S2 subunits of the Wuhan-type spike protein as substrates for selected proteases.

LC-MS/MS analysis of the TCS substrate revealed that cleavage after PS↓ (Ac-AE(E)LPDPSKPS↓KR) is a unique and preferred site for hCatK (Fig. 3A, B). This cleavage was also confirmed using the S2 subunit as a substrate for hCatK (QILPDPSKPS; Fig. 3C, D). Human CatB generated two additional cleavage products after RS↓ and SF↓ (Ac-AE(E)LPDPSKPSKRS↓F↓I) in addition to the canonical hCatB cleavage at KR↓ (Fig. 3A). In the S2 subunit analysis the RS↓ cleavage of hCatB was also confirmed. TMPRSS2 produced two expected cleavage sites: a major canonical KR↓ and a noncanonical SK↓ (Ac-AE(E)LPDPSKPSK↓R↓SFI). In contrast, hCatL, consistent with its poor proteolytic efficiency, generated only a few detectable fragments after 2h reaction.

A similar analysis was performed using the FCS-Wu and FCS-Omic substrates. Notably, hCatK exhibited a newly acquired preference for cleavage at mutation-associated sites within the FCS-Omic sequence compared to FCS-Wu, particularly at Ac-AE(E)QTKSH↓RRARSVK(D) and Ac-AE(E)QTKSHR↓RARSVK(D) (Fig. 4A,B). Furin

generated two major cleavage events in both substrates: the canonical RRAR↓ site and an additional, less expected cleavage at Q↓TNS (Ac-AE(E)Q↓TNSPRRAR↓SVK(D). Importantly, Furin, consistent with its kinetic parameters, did not exhibit any additional cleavage preferences in Omicron compared to Wuhan (Fig. 4A, C). hCatB cleaved both FCS-Wu and FCS-Omic with a similar efficacy, without a change in substrate cleavage site preference (Fig. 4A, B; Fig. S1). TMPRSS2 produced cleavage after RR↓, which overlapped with Furin (at ~50% lower intensity) and hCatB (at ~80% lower intensity). In contrast, hCatL showed minimal activity toward both FCS substrates, consistent with its poor kinetic parameters. In the S2-specific analysis, no detectable peptide fragments corresponding to the FCS were observed in the hCatL-catalyzed reactions. These results underscore hCatK and hCatB as proteases with substantial capacity to cleave both TCS and FCS sites, in contrast to the restricted specificity of TMPRSS2 and the minimal activity of hCatL. They also show that Furin and TMPRSS2 did not acquire new cleavage site preferences when comparing Wuhan and Omicron sequences. This suggests that the altered cell entry behavior of Omicron relative to Wuhan is more likely driven by a shift toward endosomal entry pathways, with a greater reliance on cathepsin-mediated activation.

Cathepsin substrate specificity towards 3CL-Mpro substrate

3CL-Mpro exhibits specificity for cleavage at the (LQ↓) motifs, which was the basis for the design of Nirmatrelvir [11,25]. Notably, LQ is also a well-recognized P2 and P1 cleavage site for cathepsins based on MEROPS database. To assess the substrate specificity of cathepsins in comparison with 3CL-Mpro, we evaluated the enzymatic kinetics of cathepsins using a 3CL-Mpro fluorogenic substrate MCA-AVLQ↓SGFR(K(Dnp)RR, and compared the kinetic parameters with those obtained for 3CL-Mpro. The results showed that hCatK (k_{cat}/K_M = 135 $mM^{-1}\ s^{-1}$) and hCatS (k_{cat}/K_M = 133 $mM^{-1}\ s^{-1}$) are about 8-fold more efficient than the viral protease (k_{cat}/K_M = 17.1 $mM^{-1}\ s^{-1}$). In contrast, hCatL and hCatB did not show any significant hydrolytic activity against the 3CL-Mpro substrate. LC-MS/MS analysis of protease cleavage sites showed that, unlike hCatL which showed trace proteolytic activity, hCatK and hCatS efficiently cleaved the 3CL-Mpro substrate at

LQ↓. In addition, hCatK also showed an expected cleavage site after FR↓ (MCA-AVLQ↓SGFR↓(K(Dnp)RR) (Fig. 5B,C,D). These findings demonstrate that both hCatK and hCatS have a strong capacity to recognize and hydrolyze the canonical 3CL-Mpro substrate at the LQ↓ motif with an efficiency substantially exceeding that of the viral protease itself.

Interaction of Nirmatrelvir with cathepsins

Given that hCatK, hCatS, and 3CL-Mpro are efficient to cleave substrates at the LQ↓ motif, we hypothesized that they might also share susceptibility to Nirmatrelvir, the inhibitor specifically designed for 3CL-Mpro [25]. To evaluate the dual inhibitory potential of Nirmatrelvir, we determined the K_i values for cathepsins. Nirmatrelvir inhibited hCatK (K_i = 600 nM) with the highest efficacy among the cathepsins tested. Cathpsin S showed an intermediate inhibition with 1.5 μM. hCatB and hCatL were not inhibited by 10 μM Nirmatrelvir (Fig. 5A). These results, together with the kinetic data and the Odanacatib-induced viral proliferation inhibition, indicate that hCatK and 3CL-Mpro represent promising targets for dual inhibition by Nirmatrelvir.

Crystal structure of hCatK/Nirmatrelvir complexes

The submicromolar inhibitory constant of Nirmatrelvir against hCatK may serve as a basis for designing more effective dual inhibitors targeting both 3CL-Mpro and hCatK. To understand how Nirmatrelvir inhibits hCatK, we determined the co-crystal structure of hCatK following covalent adduct formation with Nirmatrelvir at 1.9 Å resolution (Table S1). Nirmatrelvir binds to the active site of hCatK in a manner similar to Odanacatib, forming a covalent bond with the sulfur atom of the active site Cys25 and the nitrile group of the inhibitors (Fig. 6.C & D, Fig. S2). It also forms comparable hydrogen bonds with residues Gly66 and Asn161. The hydrogen bond between Nirmatrelvir and Gln19 of hCatK is unique when compared to the hCatK/Odanacatib complex. Well-ordered water molecules were observed in proximity to the enzyme's active site, interacting with the inhibitor. These water molecules form a hydrogen bond network involving the nitrile group, oxygen of pyrrolidine ring, and the oxygen near the 3-azabicyclo[3.1.0]hexane ring of Nirmatrelvir (Fig. 6A, shown in red), suggesting a potential role in stabilizing the inhibitor binding (Fig.

6.D). The active site of apo hCatK (PDB ID 5TUN) was aligned with the Nirmatrelvir-bound hCatK structure. Overall, the active sites appear highly similar, except for Tyr67, which is rotated 17.8° upward toward Nirmatrelvir (Fig. 6F). However, unlike Odanacatib, Nirmatrelvir lacks the π–π interaction between Tyr67 and a biphenyl ring, a key interaction present in the hCatK:Odanacatib adduct cocrystal structure (PDB 5TDI; Fig. 6G). This absence may explain the higher potency of Odanacatib, which exhibits a subnanomolar inhibition constant for hCatK (K_i = 0.18 ± 0.06 nM) [37]. Structural comparison of hCatK in its apo form and in complex with either Odanacatib or Nirmatrelvir reveals no significant conformational changes, with an RMSD of ~0.2 Å (Fig. S1; superposition was done with the all atoms), indicating that inhibitor binding does not induce major structural rearrangements. These findings suggest that incorporating a phenyl ring into the Nirmatrelvir scaffold to enable π–π stacking with Tyr67 could enhance its binding affinity and inhibitory potency toward hCatK without interfering with its binding to 3CL-Mpro.

Discussion

This study identifies hCatK as a previously unrecognized but functionally important host protease involved in SARS-CoV-2 cell entry and establishes it as a high-affinity off-target of the clinical 3CL-Mpro inhibitor, Nirmatrelvir. This is in contrast to findings where hCatL was initially identified as the primary endosomal entry facilitator for SARS and SARS-CoV-2, The supporting data, derived from CatL inhibition experiments (using both low-molecular-weight inhibitors and downregulation of CatL expression), is compromised because the inhibitors employed were often non-selective (e.g., E64-d and MDL28170) [12,38]. Furthermore, a more selective CatL inhibitor (SID26681509) exhibited an inhibitory efficacy roughly 10-fold weaker than the non-selective pan-cysteine cathepsin inhibitor, E-64d at concentrations of 10 μM [12]. In contrast, we have shown that Odanacatib, a highly potent and selective CatK had equal antiviral activity as E-64d at 10 μM.

Enzyme activity profiling revealed that hCatK cleaves Spike FCS with 25- to 70-fold higher efficiencies compared to hCatL, but is about 30 times less efficient than Furin. Strikingly, Nirmatrelvir inhibited hCatK at submicromolar concentrations (K_i = 600 nM), highlighting its potential as a dual inhibitor that targets both viral and host proteases. This dual targeting framework not only revises the protease landscape of SARS-CoV-2 entry

but also suggests new strategies for broad-spectrum antiviral intervention. The fact that an hCatB-specific inhibitor has not shown an impact on viral entry makes the enzyme irrelevant to the SARS-CoV-2 infection mechanism [39], despite its *in vitro* efficacy to cleave within the sensitive Furin and TMPRSS2 sites in the spike protein.

Considering the antiviral activity of Odanacatib, our results highlight hCatK as a key protease in viral entry, with greater functional relevance than other cathepsins. Although catalytic rates were similar between FCS-Wu and FCS-Omic, LC–MS/MS revealed distinct proteolytic patterns. The emergence of a unique cleavage site in Omicron, specifically processed by hCatK, suggests that variant-specific adaptations may alter spike processing and entry pathways. This interpretation is consistent with reports of a shift toward endosomal entry in Omicron [1]. Such adaptations underscore the importance of mapping precise cleavage events, particularly in the S2′ region adjacent to the fusion peptide, which governs membrane fusion and viral entry. For instance, the T813S (here represented within the TCS substrate: Ac-AE(E)LPDPSKP**S**KRSFIK(D)) mutation, which emerged during the evolution from SARS to SARS-CoV-2, introduces a new cleavage site at S2′ that enhances fusogenicity and infectivity [40]. Notably, we found this site to be preferentially cleaved by hCatK, suggesting a potential role for this protease in promoting syncytia formation.

Notably, the catalytic efficiency of hCatK was 7.9-fold higher than that of 3CL-Mpro when tested with the 3CL-Mpro FRET-based substrate containing the non-structural protein (NSP4-NSP5) cleavage site, LQ↓SG. LC-MS/MS analysis confirmed that hCatK was capable of efficiently cleaving at the LQ site. This is in contradiction to a previously published study stating that the LQ motif for subsite binding in the S1 and S2 is unique for 3CL-MPro [25]. The well-accepted LQ↓X cleavage site by CatK is also reflected by the significant inhibitory potency of Nirmatrelvir against this cysteine protease (K_i = 600nM), a covalent inhibitor designed to inhibit 3CL-Mpro. This finding is consistent with an earlier reported K_i value of 231 nM [41] and our co-crystal structure of hCatK and Nirmatrelvir confirms the mechanism of inhibition.

Given the restricted tissue distribution of hCatK but infection-relevant expression in lung epithelial and vascular endothelial cells [21,24] compared with the ubiquitous expression of cathepsins B and L, targeting hCatK may reduce off-target toxicity. A dual-

inhibitor approach combining 3CL-Mpro and hCatK inhibition could therefore block both viral replication and entry pathways, mitigating resistance risks inherent to single-agent therapies. This strategy is particularly relevant for spike variants such as Omicron, which rely more heavily on endosomal entry and cathepsin activity. Because treatment with hCatK inhibitors, like most antiviral regimens, is inherently short-term, adverse effects observed with long-term anti-resorptive CatK inhibition [42,43] are unlikely to be clinically relevant in the context of acute SARS-CoV-2 infections.

While our findings provide functional and structural evidence implicating hCatK in SARS-CoV-2 infection, further validation in physiologically relevant *in vivo* models is necessary. Additionally, detailed studies on protease expression profiles and viral tropism across cell types will refine the therapeutic potential of hCatK targeting. Future work should also examine other viral infections, such as Ebola virus, where cell entry depends on cathepsins and convertases [44], and focus on optimizing dual inhibitors to improve potency and selectivity based on the structural framework established here. Together, our results shift the focus toward hCatK and not hCatL as a critical host protease in SARS-CoV-2 pathogenesis and establish a foundation for rational design of dual inhibitors. This integrative approach combining enzymatic kinetics, structural biology, and functional validation advances the understanding of host-virus interactions and informs next-generation antiviral strategies.

References:

1. Willett, B.J. et al. Publisher Correction: SARS-CoV-2 Omicron is an immune escape variant with an altered cell entry pathway. *Nat Microbiol* **7**, 1709 (2022).
2. Hachmann, N.P. et al. Neutralization Escape by SARS-CoV-2 Omicron Subvariants BA.2.12.1, BA.4, and BA.5. *N Engl J Med* **387**, 86-88 (2022).
3. Planas, D. et al. Considerable escape of SARS-CoV-2 Omicron to antibody neutralization. *Nature* **602**, 671-675 (2022).
4. Qing, E., Salgado, J., Wilcox, A. & Gallagher, T. SARS-CoV-2 Omicron variations reveal mechanisms controlling cell entry dynamics and antibody neutralization. *PLoS Pathog* **20**, e1012757 (2024).

5. Yin, X. et al. Global siRNA screen identifies human host factors critical for SARS-CoV-2 replication and late stages of infection. *PLoS Biol* **23**, e3002738 (2025).
6. Israeli, M. et al. Genome-wide CRISPR screens identify GATA6 as a proviral host factor for SARS-CoV-2 via modulation of ACE2. *Nat Commun* **13**, 2237 (2022).
7. Pahmeier, F. et al. Identification of host dependency factors involved in SARS-CoV-2 replication organelle formation through proteomics and ultrastructural analysis. *J Virol* **97**, e0087823 (2023).
8. Aw, D.Z.H., Zhang, D.X. & Vignuzzi, M. Strategies and efforts in circumventing the emergence of antiviral resistance against conventional antivirals. *NPJ Antimicrob Resist* **3**, 54 (2025).
9. Shang, J. et al. Cell entry mechanisms of SARS-CoV-2. *Proc Natl Acad Sci U S A* **117**, 11727-11734 (2020).
10. Jackson, C.B., Farzan, M., Chen, B. & Choe, H. Mechanisms of SARS-CoV-2 entry into cells. *Nat Rev Mol Cell Biol* **23**, 3-20 (2022).
11. Hoffman, R.L. et al. Discovery of Ketone-Based Covalent Inhibitors of Coronavirus 3CL Proteases for the Potential Therapeutic Treatment of COVID-19. *J Med Chem* **63**, 12725-12747 (2020).
12. Zhao, M.M. et al. Cathepsin L plays a key role in SARS-CoV-2 infection in humans and humanized mice and is a promising target for new drug development. *Signal Transduct Target Ther* **6**, 134 (2021).
13. Shapira, T. et al. A TMPRSS2 inhibitor acts as a pan-SARS-CoV-2 prophylactic and therapeutic. *Nature* **605**, 340-348 (2022).
14. Papa, G. et al. Furin cleavage of SARS-CoV-2 Spike promotes but is not essential for infection and cell-cell fusion. *Plos Pathogens* **17**(2021).
15. Essalmani, R. et al. Distinctive Roles of Furin and TMPRSS2 in SARS-CoV-2 Infectivity. *J Virol* **96**, e0012822 (2022).
16. Scarcella, M. et al. The Key Role of Lysosomal Protease Cathepsins in Viral Infections. *Int J Mol Sci* **23**(2022).
17. Sacco, M.D. et al. Structure and inhibition of the SARS-CoV-2 main protease reveal strategy for developing dual inhibitors against saMpro and cathepsin L. *Science Advances* **6**(2020).

18. Ma, X.R. et al. MPI8 is Potent against SARS-CoV-2 by Inhibiting Dually and Selectively the SARS-CoV-2 Main Protease and the Host Cathepsin L. *ChemMedChem* **17**, e202100456 (2022).
19. Costanzi, E. et al. Structural and Biochemical Analysis of the Dual Inhibition of MG-132 against SARS-CoV-2 Main Protease (Mpro/3CLpro) and Human Cathepsin-L. *Int J Mol Sci* **22**(2021).
20. Riva, L. et al. Discovery of SARS-CoV-2 antiviral drugs through large-scale compound repurposing. *Nature* **586**, 113-119 (2020).
21. Bühling, F. et al. Expression of cathepsin K in lung epithelial cells. *Am J Respir Crit Care Med* **20**, 612-619 (1999).
22. Buhling, F. et al. Lysosomal cysteine proteases in the lung: role in protein processing and immunoregulation. *Eur Respir J* **23**, 620-8 (2004).
23. Buhling, F. et al. Expression of cathepsins B, H, K, L, and S during human fetal lung development. *Dev Dyn* **225**, 14-21 (2002).
24. Platt, M.O. et al. Expression of cathepsin K is regulated by shear stress in cultured endothelial cells and is increased in endothelium in human atherosclerosis. *Am J Physiol Heart Circ Physiol* **292**, H1479-86 (2007).
25. Owen, D.R. et al. An oral SARS-CoV-2 M(pro) inhibitor clinical candidate for the treatment of COVID-19. *Science* **374**, 1586-1593 (2021).
26. Linnevers, C.J. et al. Expression of human cathepsin K in *Pichia pastoris* and preliminary crystallographic studies of an inhibitor complex. *Protein Science* **6**, 919-921 (1997).
27. Andrault, P.M., Panwar, P. & Bromme, D. Characterization of cathepsin S exosites that govern its elastolytic activity. *Biochem J* **477**, 227-242 (2020).
28. Fraser, B.J. et al. Structure and activity of human TMPRSS2 protease implicated in SARS-CoV-2 activation. *Nat Chem Biol* **18**, 963-971 (2022).
29. Battye, T.G., Kontogiannis, L., Johnson, O., Powell, H.R. & Leslie, A.G. iMOSFLM: a new graphical interface for diffraction-image processing with MOSFLM. *Acta Crystallogr D Biol Crystallogr* **67**, 271-81 (2011).
30. Winn, M.D. et al. Overview of the CCP4 suite and current developments. *Acta Crystallogr D Biol Crystallogr* **67**, 235-42 (2011).

31. Moriarty, N.W., Grosse-Kunstleve, R.W. & Adams, P.D. Electronic Ligand Builder and Optimization Workbench (eLBOW): a tool for ligand coordinate and restraint generation. *Acta Crystallogr D Biol Crystallogr* **65**, 1074-80 (2009).
32. Adams, P.D. et al. PHENIX: a comprehensive Python-based system for macromolecular structure solution. *Acta Crystallogr D Biol Crystallogr* **66**, 213-21 (2010).
33. Emsley, P., Lohkamp, B., Scott, W.G. & Cowtan, K. Features and development of Coot. *Acta Crystallogr D Biol Crystallogr* **66**, 486-501 (2010).
34. Matarese, A., Gambardella, J., Sardu, C. & Santulli, G. miR-98 Regulates TMPRSS2 Expression in Human Endothelial Cells: Key Implications for COVID-19. *Biomedicines* **8**(2020).
35. Wagner, J.U.G. et al. Increased susceptibility of human endothelial cells to infections by SARS-CoV-2 variants. *Basic Res Cardiol* **116**, 42 (2021).
36. Lavie, M., Dubuisson, J. & Belouzard, S. SARS-CoV-2 Spike Furin Cleavage Site and S2' Basic Residues Modulate the Entry Process in a Host Cell-Dependent Manner. *J Virol* **96**, e0047422 (2022).
37. Law, S. et al. Identification of mouse cathepsin K structural elements that regulate the potency of odanacatib. *Biochem J* **474**, 851-864 (2017).
38. Simmons, G. et al. Inhibitors of cathepsin L prevent severe acute respiratory syndrome coronavirus entry. *Proc Natl Acad Sci U S A* **102**, 11876-81 (2005).
39. Ou, X.Y. et al. Characterization of spike glycoprotein of SARS-CoV-2 on virus entry and its immune cross-reactivity with SARS-CoV. *Nature Communications* **11**(2020).
40. Ma, Y. et al. Spike substitution T813S increases Sarbecovirus fusogenicity by enhancing the usage of TMPRSS2. *PLoS Pathog* **19**, e1011123 (2023).
41. Duveau, D.Y. & Thomas, C.J. The Remarkable Selectivity of Nirmatrelvir. *ACS Pharmacol Transl Sci* **5**, 445-447 (2022).
42. Runger, T.M. et al. Morphea-like skin reactions in patients treated with the cathepsin K inhibitor balicatib. *J Am Acad Dermatol* **66**, e89-96 (2012).
43. Mullard, A. Merck &Co. drops osteoporosis drug odanacatib. *Nat Rev Drug Discov* **15**, 669 (2016).

44. Bestle, D. et al. Novel proteolytic activation of Ebolavirus glycoprotein GP by TMPRSS2 and cathepsin L at an uncharted position can compensate for furin cleavage. *Virus Res* **347**, 199430 (2024).

Author contributions: SJTD, DS, PP, and DB designed the study, validated results, and were responsible for the administration of project. Specifically, SJTD performed substrate kinetics and all LC-MS/MS analyses and OH executed sample preparation for LC-MS/MS. DS also performed substrate kinetics and was responsible together with FvP and YSC for the crystallization and structural analysis of the CatK/Nirmatrelvir complex. MN performed all BSL3 SARS-CoV-2 endothelial infection experiments and PP was responsible for all cell-based analyses. EM produced and purified recombinant human cathepsin K. SYTD produced and purified human cathepsin S. DS and SYTD produced and purified SARS-CoV-2 3CL-Mpro. BJF and CA produced recombinant TMPRSS2. SJTD, DS, and DB wrote the original draft of the manuscript. All authors reviewed and revised the final manuscript. DB acquired funding for the study.

Acknowledgements: This work was supported by Canadian Institutes of Health Research grants (PJT-155979, CPG-158275), Collaborative Health Research Project (NSERC CHRP 523434-18) and the NSERC discovery grant (LJGP GR003266). DB was supported by Canada Research Chair award funding. We are thankful to the proteomics core facility at UBC under the leadership of L. Foster and the technical support by J. Rogalski to generate the raw LC-MS/MS data.

Conflict of interest statement: No disclosures and all authors have no conflicts of interest.

Figure legends

Figure 1: Infection-induced upregulation of CatK and antiviral effects of protease inhibitors in EA.hy926 endothelial cells. (A–B) Immunofluorescence images showing Actin (green, Phalloidin), nuclei (blue, DAPI), and CatK (red) in uninfected control (A) and infected (B) EA.hy926 cells. Infection leads to increased CatK expression and altered cytoskeletal morphology. Scale bar: 100 µm. (C) Quantification of CatK expression (fold change) in control vs. infected cells. Data are shown as mean ± SEM (n = 4); ***$p < 0.001$. (D) Immunostaining for viral nucleocapsid protein (yellow) and actin (green) after treatment with Nirmatrelvir (2.5 µM), Camostat (10 µM), E-64d (10 µM), and Odanacatib (10 µM). (E) Dose-dependent inhibition of intracellular nucleocapsid levels by the four compounds. Data represent mean ± SEM (n = 3). (F) EC_{50} values of the tested compounds calculated from the dose-response curves in (E).

Figure 2: Kinetic analysis of the cleavage activities of human cathepsins and TMPRSS2 and Furin at S1/S1 and S2' cleavage site areas in SARS-CoV-2 Spike protein. (A) Schematic representation of the Spike (S) protein, highlighting the Furin and TMPRSS2 cleavage sites. The amino acid sequences of S proteins from various SARS-related coronaviruses are aligned for comparison. (B) Table compares the kinetic parameters of selected cysteine cathepsins toward FCS-Wu and FCS-Omic substrates. (C) Table compare the kinetic parameters of Furin and TMPRSS2 using two fluorogenic substrates derived from the S1/S2 site: FCS-Wu (Ac-AE(Edans)QTNSPRRARSVK(Dabcyl)) and FCS-Omic (Ac-AE(Edans)QTKSHRRARSVK(Dabcyl)). (D) Table compare the kinetic parameters of Furin, TMPRSS2, and selected cysteine cathepsins using the synthetic fluorogenic substrate TCS (Ac-AE(Edans)LPDPSKPSKRSFIK(Dabcyl). The kinetic data were obtained from two independent experiments, each performed in triplicate. Values are reported as mean ± standard deviation (SD).

Figure 3: Cleavage site analysis in TMPRSS2 sensitive areas of Spike protein derived substrates. (A) Comparing the relative peak area (%) of proteases cleavage products using TCS as a substrate. (B) The tandem mass spectrum of a selected product peptide (Ac-AE(Edans)LPPSKPS. (C) Comparing proteases cleavage products in S2'

region using recombinant spike protein as a substrate. (D) The tandem mass spectrum of a selected product peptide QILPDPSKPS. Peptides are shown in their full-length sequences; underlined regions indicate fragments that were detected and confirmed by LC-MS/MS. The data were obtained from two independent replicates. Values are reported as mean ± standard deviation (SD).

Figure 4: Cleavage site analysis in Furin sensitive areas of Spike protein derived substrates. Comparing the relative peak area (%) of proteases cleavage products using FCS-Wu (A) and FCS-Omic (B) as a substrate. (C) The tandem mass spectrum of a selected product peptide TNSPRRAR. (D) Comparing proteases cleavage products in S1/S2 region using recombinant spike protein as a substrate. Peptides are shown in their full-length sequences; underlined regions indicate fragments that were detected and confirmed by LC-MS/MS. The data were obtained from two independent replicates. Values are reported as mean ± standard deviation (SD).

Figure 5: Kinetic and cleavage site analysis of human cathepsins and 3CL-Mpro of a substrate representing the NSP4-NSP5 processing site and their K_i values towards Nirmatrelvir. (A) Table compare the kinetic parameters of cathepsins and 3CL-Mpro using a standard 3CL-Mpro substrate (MCA-AVLQSGFRK(Dnp)RR). (B) Comparing the relative peak area (%) of cathepsins cleavage products using 3CL substrate. (C) mass spectrum of MCA-AVLQ which a major product of 3CL and hCatK and hCatS. (D) tandem mass spectrum of MCA-AVLQ. Peptides are shown in their full-length sequences; underlined regions indicate fragments that were detected and confirmed by LC-MS/MS. The kinetic data were obtained from two independent experiments, each performed in triplicate. Values are reported as mean ± standard deviation (SD).

Figure: 6. Crystal structure of hCatK with Nirmatrelvir. Structures of A) Nirmatrelvir and (B) Odanacatib (C) Nirmatrelvir bound at the active site of hCatK. (D) Polar interaction

of Nirmatrelvir with active site amino acids (*cyan*) and water (*red*) shown in *magenta*. (E) Omit map of Nirmatrelvir contoured at σ 3. (F) Comparison of the active site of hCatK in the presence and absence of Nirmatrelvir. Uninhibited hCatK shown in *palegreen*; Nirmatrelvir (white colour) bound hCatK and water molecules were shown in *cyan.* (G) Comparison of active site of hCatK bound to Odanacatib and Nirmtrelvir. Odanacatib bound hCatK and water molecules were shown in *deepsalmon;* Polar interaction of Odanacatib shown in *yellow.*

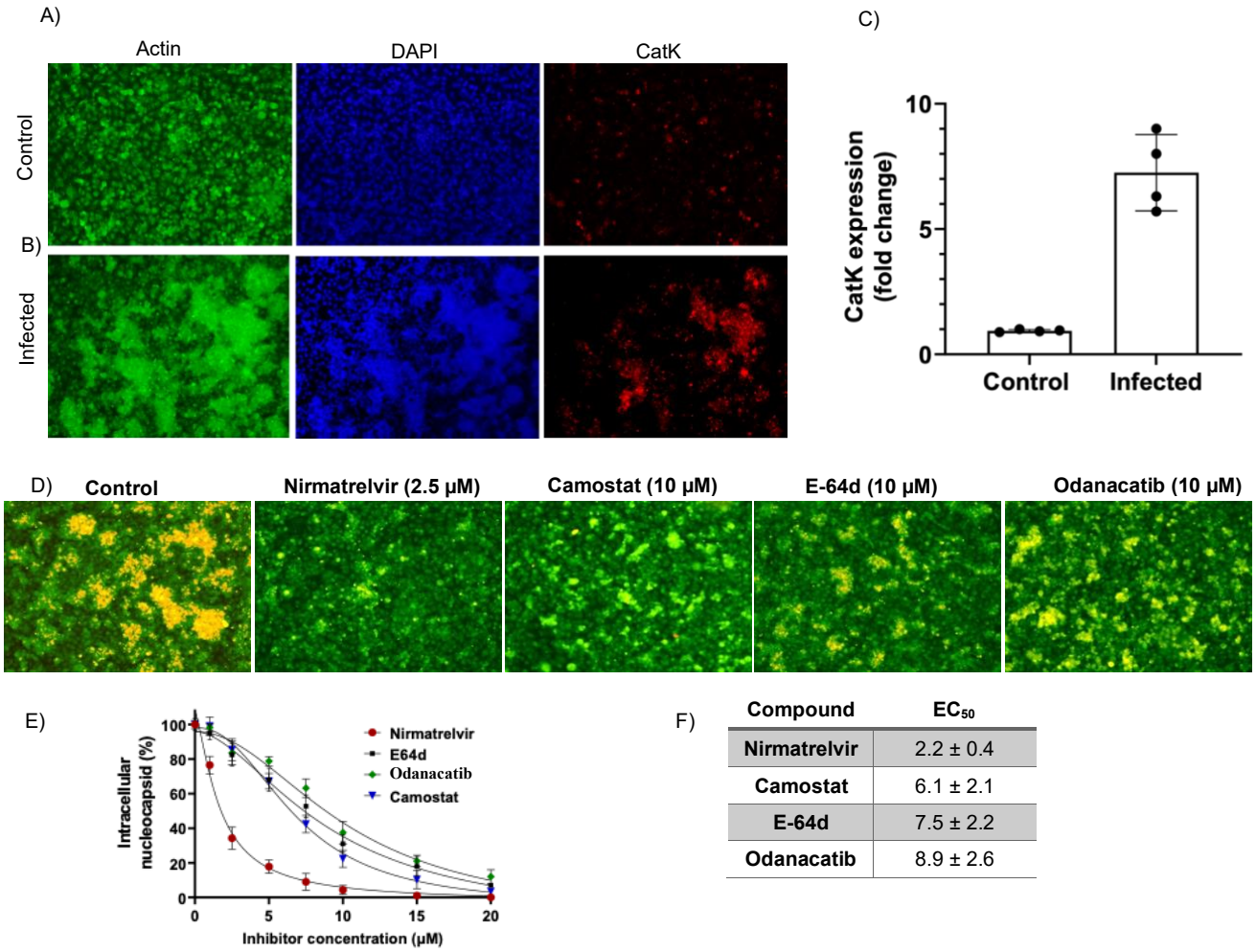

Compound	EC_{50}
Nirmatrelvir	2.2 ± 0.4
Camostat	6.1 ± 2.1
E-64d	7.5 ± 2.2
Odanacatib	8.9 ± 2.6

Figure 1

A)

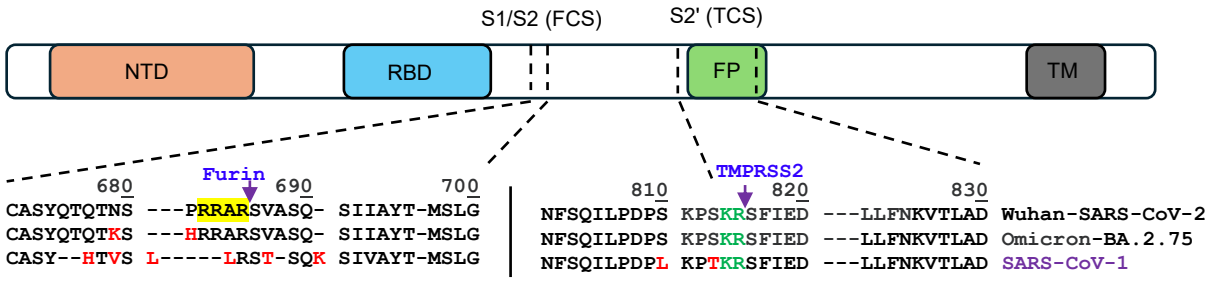

B)

FCS-Wu Ac-AE(Edans)QTNSPRRARSVK(Dabcyl)
FCS-Omic Ac-AE(Edans)QTKSHRRARSVK(Dabcyl)

Enzyme	**hCatB**	**hCatB**	**hCatK**	**hCatK**	**hCatS**	**hCatS**	**hCatL**	**hCatL**
Substrate	FCS-Wu	FCS-Omic	FCS-Wu	FCS-Omic	FCS-Wu	FCS-Omic	FCS-Wu	FCS-Omic
K_M *(μM)*	22 ± 2.7	12.8 ± 3.3	18.3 ± 3	16.2 ± 1.9	29.9 ± 5.7	20.6 ± 5.7	4.2 ± 1.9	3 ± 0.5
k_{cat} *(s^{-1})*	4.8 ± 0.3	3.4 ± 0.3	1.4 ± 0.08	0.9 ± 0.04	0.04 ± 0.004	0.008 ± 0.0007	0.005 ± 0.0008	0.007 ± 0.0003
k_{cat}/K_M *(mM^{-1} s^{-1})*	218	265	76	55	1.3	0.4	1.2	2.3

C)

Enzyme	**Furin**	**Furin**	**TMPRSS2**	**TMPRSS2**
Substrate	FCS-Wu	FCS-Omic	FCS-Wu	FCS-Omic
K_M *(μM)*	9.7 ± 2	8.3 ± 2	38.2 ± 4.2	21.6 ± 3.5
k_{cat} *(s^{-1})*	22.2 ± 1.3	24.7 ± 1.5	10.6 ± 0.5	6.5 ± 0.3
k_{cat}/K_M *(mM^{-1} s^{-1})*	2288	2976	277	300

D)

TCS Ac-AE(Edans)LPDPSKPSKRSFIK(Dabcyl)

Enzyme	**TMPRSS2**	**Furin**	**hCatB**	**hCatK**	**hCatS**	**hCatL**
Substrate	TCS	TCS	TCS	TCS	TCS	TCS
K_M *(μM)*	30 ± 6	Trace Activity	11.2 ± 2	48.3 ± 24	6.7 ± 2	Trace Activity
k_{cat} *(s^{-1})*	2.7 ± 0.2	Trace Activity	1.9 ± 0.1	1.2 ± 0.4	0.05 ± 0.07	Trace Activity
k_{cat}/K_M *(mM^{-1} s^{-1})*	90	Trace Activity	170	24	7.4	Trace Activity

Figure 2

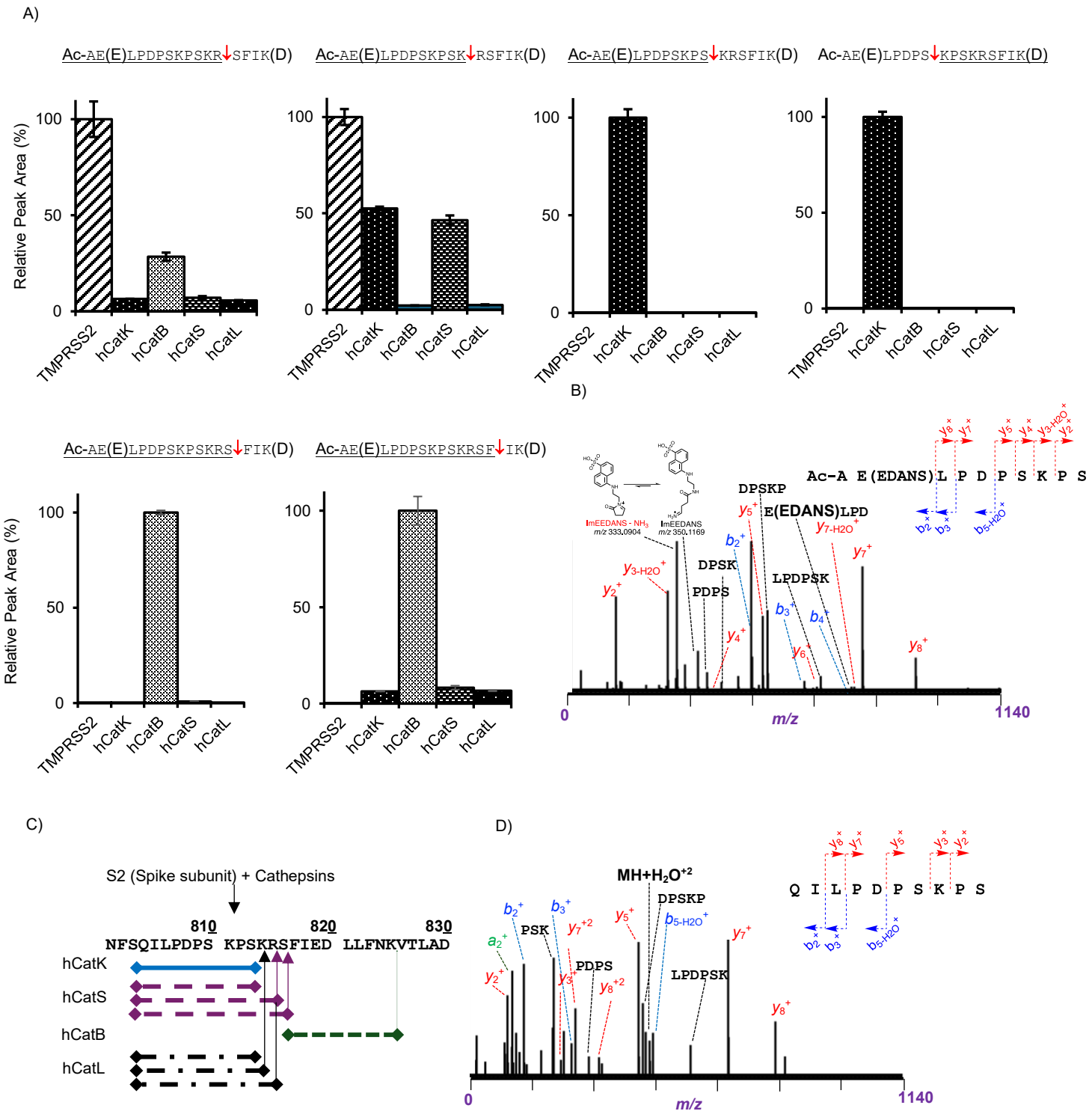
A)
Ac-AE(E)LPDPSKPSKR↓SFIK(D)
Ac-AE(E)LPDPSKPSK↓RSFIK(D)
Ac-AE(E)LPDPSKPS↓KRSFIK(D)
Ac-AE(E)LPDPS↓KPSKRSFIK(D)
Relative Peak Area (%)
100
50
0
TMPRSS2
hCatK
hCatB
hCatS
hCatL
B)
Ac-AE(E)LPDPSKPSKRS↓FIK(D)
Ac-AE(E)LPDPSKPSKRSF↓IK(D)
ImEEDANS - NH3
m/z 333.0904
ImEEDANS
m/z 350.1169
Ac-A E(EDANS)L P D P S K P S
DPSKP
E(EDANS)LPD
DPSK
PDPS
LPDPSK
m/z
0
1140
C)
S2 (Spike subunit) + Cathepsins
810
820
830
NFSQILPDPS KPSKRSFIED LLFNKVTLAD
hCatK
hCatS
hCatB
hCatL
D)
MH+H2O+2
DPSKP
PSK
PDPS
LPDPSK
Q I L P D P S K P S
m/z
0
1140

Figure 3

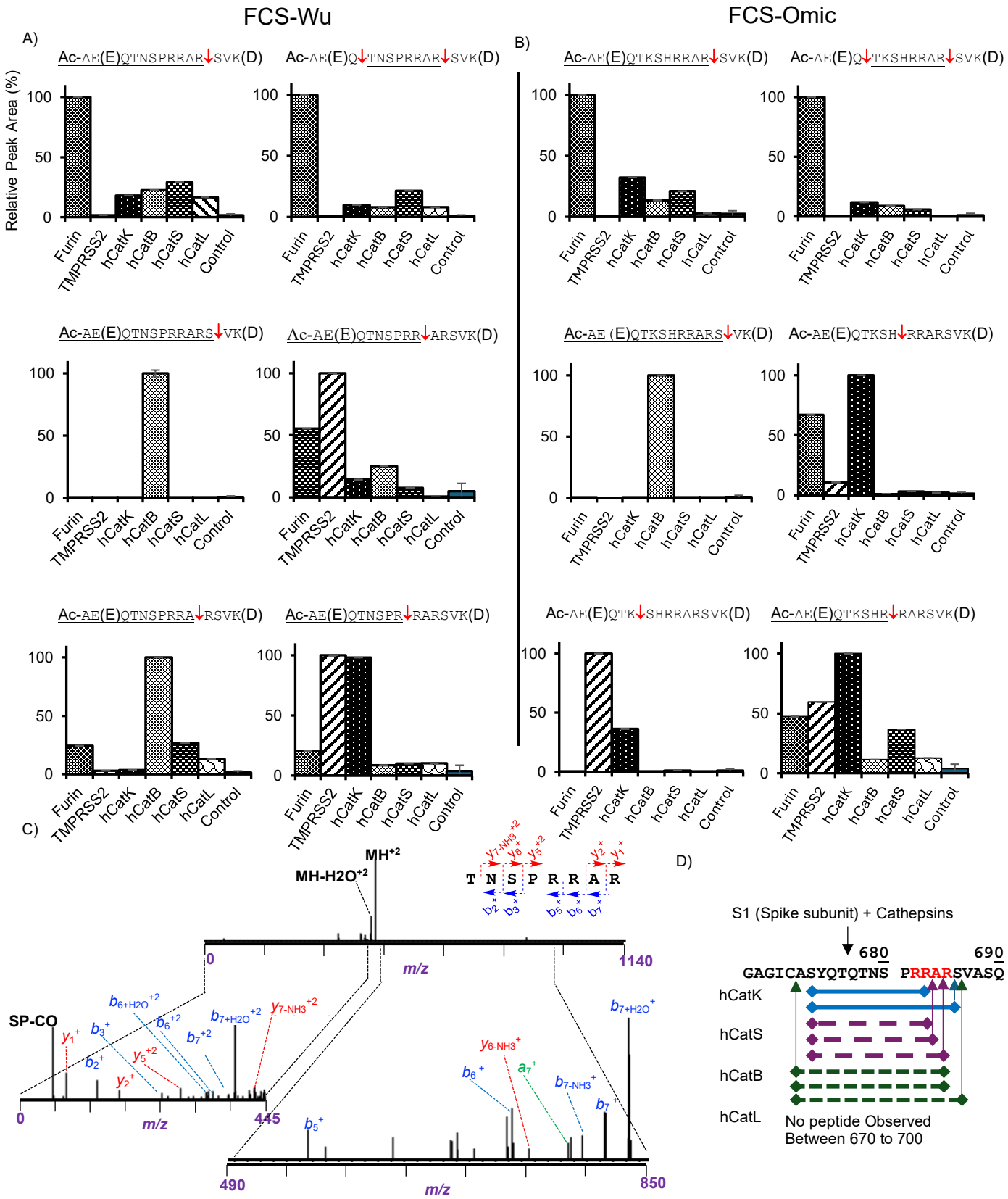
FCS-Wu
FCS-Omic
A)
B)
C)
D)
Relative Peak Area (%)
Ac-AE(E)QTNSPRRAR↓SVK(D)
Ac-AE(E)Q↓TNSPRRAR↓SVK(D)
Ac-AE(E)QTNSPRRARS↓VK(D)
Ac-AE(E)QTNSPRR↓ARSVK(D)
Ac-AE(E)QTNSPRRA↓RSVK(D)
Ac-AE(E)QTNSPR↓RARSVK(D)
Ac-AE(E)QTKSHRRAR↓SVK(D)
Ac-AE(E)Q↓TKSHRRAR↓SVK(D)
Ac-AE (E)QTKSHRRARS↓VK(D)
Ac-AE(E)QTKSH↓RRARSVK(D)
Ac-AE(E)QTK↓SHRRARSVK(D)
Ac-AE(E)QTKSHR↓RARSVK(D)
Furin
TMPRSS2
hCatK
hCatB
hCatS
hCatL
Control
MH+2
MH-H2O+2
SP-CO
m/z
S1 (Spike subunit) + Cathepsins
680
690
GAGICASYQTQTNS PRRARSVASQ
hCatK
hCatS
hCatB
hCatL
No peptide Observed
Between 670 to 700

Figure 4

A)

Enzyme	hCatL	hCatB	hCatS	hCatK	3CL-M^{pro}
Substrate	3CL-Sub	3CL-Sub	3CL-Sub	3CL-Sub	3CL-Sub
K_M *(μM)*	Trace Activity	Trace Activity	21 ± 4	9.6 ± 2	35 ± 10
k_{cat} *(s^{-1})*	Trace Activity	Trace Activity	2.8 ± 0.2	1.3 ± 0.1	0.6 ± 0.1
k_{cat}/K_M *(mM^{-1} s^{-1})*	Trace Activity	Trace Activity	133	135	17
K_i *(μM) Nirmatrelvir*	N/A	N/A	1.5 ± 0.2	0.6 ± 0.1	0.035 ± 0.014

B)

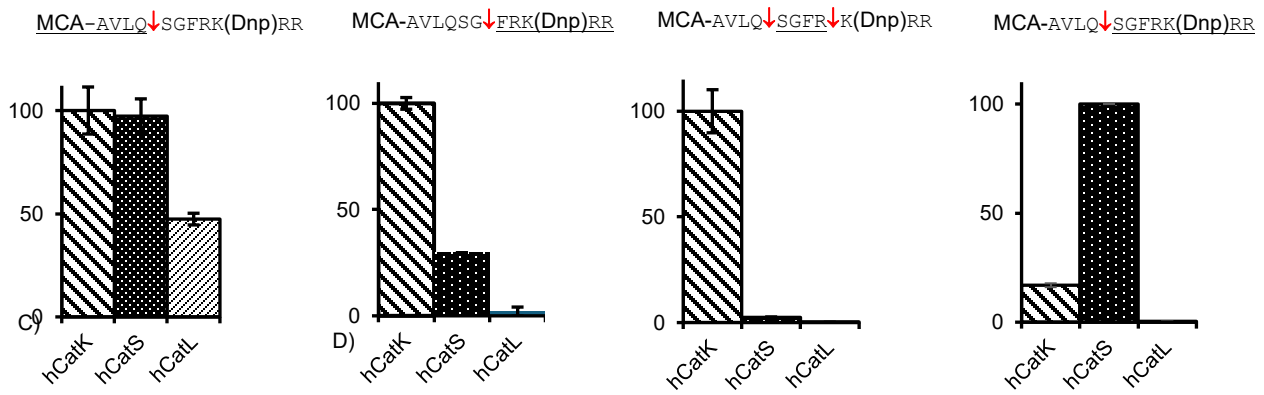

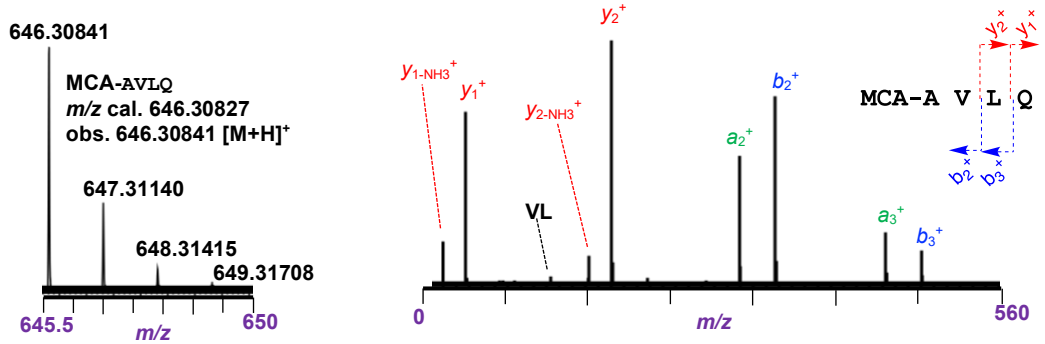

Figure 5

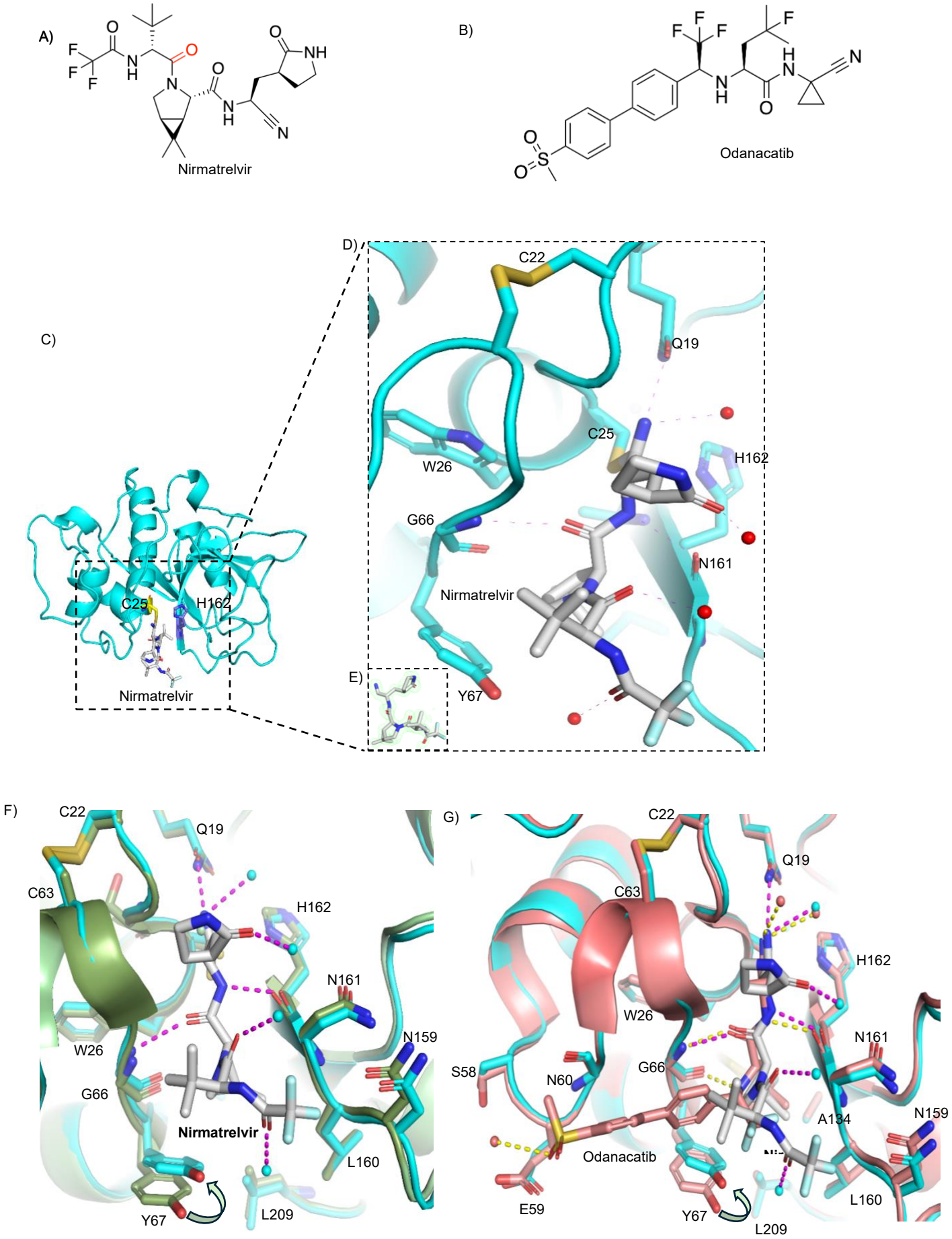
A)
Nirmatrelvir
B)
Odanacatib
C)
C25
H162
Nirmatrelvir
D)
C22
Q19
C25
H162
W26
G66
N161
Nirmatrelvir
Y67
E)
F)
C22
Q19
C63
H162
N161
N159
W26
G66
Nirmatrelvir
L160
Y67
L209
G)
C22
Q19
C63
H162
W26
N161
S58
N60
G66
A134
N159
Odanacatib
E59
Y67
L160
L209

Figure 6